

# Structure detection in the D1 CFHTLS deep field using accurate photometric redshifts: a benchmark

A. Mazure<sup>1</sup>, C. Adami<sup>1</sup>, M. Pierre<sup>2</sup>, O. Le Fèvre<sup>1</sup>, S. Arnouts<sup>1</sup>, P. A. Duc<sup>2</sup>, O. Ilbert<sup>3</sup>, V. LeBrun<sup>1</sup>, B. Meneux<sup>1,4,5</sup>, F. Pacaud<sup>2</sup>, J. Surdej<sup>3</sup>, and I. Valtchanov<sup>6</sup>

<sup>1</sup> LAM, Traverse du siphon 13012 Marseille, France

<sup>2</sup> DAPNIA/SAP, CEA Saclay, 91191 Gif sur Yvette, France

<sup>3</sup> Institut d'Astrophysique et de Géophysique, Université de Liège, Allée du 6 Août, 17, B5C, B-4000 Sart Tilman, Belgique

<sup>4</sup> INAF - IASF, Via Bassini 15, I-20133 Milano, Italy

<sup>5</sup> INAF, Osservatorio Astronomico di Brera, Via Bianchi 46, I-23807 Merate (LC), Italy

<sup>6</sup> Herschel Science Centre, ESA, European Space Astronomy Centre (ESAC), Villafranca del Castillo, PO Box 50727, Madrid 28080, Spain

Received 2006; accepted ????

## ABSTRACT

*Aims.* We investigate structures in the D1 CFHTLS deep field in order to test the method that will be applied to generate homogeneous samples of clusters and groups of galaxies in order to constrain cosmology and detailed physics of groups and clusters.

*Methods.* Adaptive kernel technique is applied on galaxy catalogues. This technique needs none of the usual a-priori assumptions (luminosity function, density profile, colour of galaxies) made with other methods. Its main drawback (decrease of efficiency with increasing background) is overcome by the use of narrow slices in photometric redshift space. There are two main concerns in structure detection. One is false detection and the second, the evaluation of the selection function in particular if one wants "complete" samples. We deal here with the first concern using "random" distributions. For the second, comparison with detailed simulations is foreseen but we use here a pragmatic approach with comparing our results to GalICS simulations to check that our detection number is not totally at odds compared to cosmological simulations. We use XMM-LSS survey and secured VVDS redshifts up to  $z \sim 1$  to check individual detections.

*Results.* We show that our detection method is basically capable to recover (in the regions in common) 100% of the C1 XMM-LSS X-ray detections in the correct redshift range plus several other candidates. Moreover when spectroscopic data are available, we confirm our detections, even those without X-ray data.

**Key words.** cosmology – clusters – groups

## 1. Introduction

Considering groups and clusters of galaxies as "cosmological probes", two questions are still presently asked: when these structures were formed and could they constrain model-universes if we count them consistently with redshift and mass? Obviously, both questions point out for the need of "complete" samples of clusters and groups to answer them. Moreover, once such samples are available, detailed physics of galaxy groups and clusters can be studied.

With the CFHTLS survey (Canada-France Hawaii Telescope Legacy Survey, see <http://www.cfht.hawaii.edu/Science/CFHTLS>) this could be done up to  $z \geq 1$  extending e.g. recent GEMS study (Forbes et al. 2006) on nearby groups.

Physically, groups and clusters are deep gravitational potential wells containing together dark matter, hot gas and galax-

ies. Each of these components could then in principle be used to detect their parent host.

a) Dark matter (DM hereafter): this phase is usually sampled via lensing studies (e.g. Gavazzi et al 2006 on the same CFHTLS fields and references herein), since DM traces directly the mass. However, lensing detection is efficient up to not too high  $z$  systems (Hamana et al 2003), due to projection effects and lack of sensitivity to small groups. Moreover due to the complex mass distribution of DM haloes and the spoiling influence of intrinsic alignments of galaxies, lensing-selected clusters could not be really mass-selected (e.g. Tang & Fan 2005).

b) Hot gas: this can be achieved in two ways. First, X-rays (e.g. Pierre et al. 2006 and references therein) in principle probe gravitational wells without projection effects, but are contaminated by line of sight stars or active galaxies. Limited exposure times also become problematic for faint remote clusters. Second, the Sunyaev-Zeldovich (SZ hereafter) technique

works at any redshift but in practice there are limitations for distant objects due to the lack of spatial resolution.

c) Galaxies: First, for this component, spectroscopic redshift surveys are in principle the optimal tool since they probe directly the dynamics of the systems. Most of the time, however, the spatial sampling is partial and not homogeneous. Moreover, high redshift clusters are not well probed due to slits/fibers overlap problems. Second, pure photometric catalogs can be used, searching for galaxy overdensities over the sky. This method provides in general an homogeneous spatial coverage, but the contrast of structures decreases rapidly with redshift with respect to the total background. Improvements are possible for example by using matching filter technics (Postman et al 1996 for the seminal work, Olsen et al 2007 on the CFHTLS fields) and/or selecting galaxies on a colour-basis (using red sequence in the colour magnitude relation e.g. Gladders and Yee 2000, 2005) but this method is possibly introducing a bias in the sense that it searches only for clusters exhibiting such a relation. Moreover, even if the colour magnitude relation already seems to be in place up to  $z \sim 1.5$  (e.g Cucciati et al. 2006 for a complete discussion), the colour-magnitude distribution dependence upon environment also varies with redshift. So, one would have ideally to adapt the cluster search using the colour magnitude relation not only to the redshift but also to the local density. This kind of improvement was also generalized in Miller et al. (2005), identifying clusters of galaxies as overdensities in a seven-dimensional position and color space to minimize the projection effects.

We chose a similar way to solve the problem of lack of contrast in using photometric redshifts to define redshift slices. But, up to now, the accuracy of such redshifts was moderate and significant numbers of totally wrong redshift estimates were still present.

However, impressive improvements have been recently performed due to training of spectral templates and calibration with very good and large spectroscopic samples over large range of redshifts and down to similar magnitude depth compared to the photometric catalogs. We therefore used such improved photometric redshifts (Ilbert et al. 2006) in order to define redshift slices which allows to increase the contrast when computing galaxy density maps. This results in an homogeneous sample (besides masked photometric areas) only limited by the photometric catalog depth.

We took advantage of both excellent multi wavelength photometry from CFHTLS and very large samples of spectra (VVDS survey: VIMOS VLT Deep Survey, Le Fèvre et al. 2005) to define these very good photometric redshifts in the CFHTLS D1 field and, here, we exploit them to search for structures in that field. We postpone to another paper, in which all the CFHTLS fields will be analysed, the use of counts of structures to constrain cosmological parameters. Indeed, only a few systems are expected in less than 1 square degree. Rather, we stress here on how the method appears efficient. In particular, a close comparison to the X-ray detections done in the frame of the XMM-LSS survey (e.g. Pierre et al. 2006) shows a very good agreement when taking into account biases in both methods and we will also detail this comparison using secured VVDS redshifts.

Section 2 is about data and methods. Section 3 describes the structure detection and results reliability. Finally, Section 4 is the conclusion.

All along that paper we use the following cosmological parameters:  $H_0 = 67 \text{ km.s}^{-1}.\text{Mpc}^{-1}$ ,  $\Omega_\Lambda = 0.67$  and  $\Omega_m = 0.33$  in order to be coherent with the GalICS simulations we used.

## 2. Data and method

### 2.1. CFHTLS photometric data and photometric redshifts

The catalogues (publicly available and fully described at <http://terapix.iap.fr>) used for the detection and the characterization of the structures have been obtained within the frame of the CFHT Legacy Survey (i.e MEGACAM  $u^*$ ,  $g'$ ,  $r'$ ,  $i'$ ,  $z'$  data) for the so-called D1 deep field. We will use the  $i'$  band to detect our structures (see below).

For the photometric redshift calculations, photometry (BVRI) obtained in the frame of the VVDS survey (Le Fèvre et al 2005) as well as Spitzer data are also used (see Ilbert et al. 2006 for details). In a few words, photometric redshifts are obtained by adjusting Spectral Energy Distribution of galaxy templates which are iteratively modified in terms of flux zero points and continua shapes using a set of high quality spectroscopic redshifts issued from the VVDS (see Ilbert et al 2006). A very good accuracy is obtained between  $z = 0.2$  and  $z=1.2$  and for  $i' = 24.5$  (the present limit of our sample, see below) as described in Ilbert et al. (2006): in a photometric/spectroscopic redshift plot, the standard deviation is 0.04 in redshift.

### 2.2. The VVDS spectroscopic data and XMM data

On one hand, once the structures are identified with their galaxy content (see following sections), we look for spectroscopic data in the VVDS catalogue both to confirm or not our detections and to give if possible an estimate of the velocity dispersion. However, the VVDS does not cover the entire D1 field and is characterized by an inhomogeneous sampling rate and avoid peculiar masked regions (distinct from the CFHTLS D1 masked regions however). So, several systems have only a few or no spectroscopic measurements at all.

On the other hand, the XMM-LSS (Pierre et al. 2006) provides for the CFHTLS D1 covered area, a catalog of candidate structures classified in several classes (C1, C2, C3) with confirmed spectroscopic redshifts (independently from VVDS redshifts).

Class 1 (C1) is defined as sources with no contamination of misclassified point sources as extended ones. Class 2 (C2) corresponds to a contamination of 50% and class 3 (C3) highly contaminated ones (see Pierre et al 2006 for more details). We use also the identifications done by Willis et al. (2005) and Andreon et al. (2005) of specific systems with the same X-ray data.

First of all, Fig. 1 shows the CFHTLS D1 masked regions due to bright stars and CCD defects of the optical data. Masked regions are represented by the spurious objects that were detected inside. Rings made by agglomerated points with empty

**Fig. 1.** Masked regions following the CFHTLS recipe on the D1 field with the XMM detections superimposed. Red filled squares are the C1 XMM-LSS clusters and blue ones are the C2 and C3. We also give the name of the XMM-LSS cluster (see Pierre et al. 2006) as well as its redshift and bolometric X-ray luminosity in  $10^{44}$  erg/s within  $R_{500}$ .  $\alpha$  and  $\delta$  are given in decimal degrees.

centers are for example due to stars that shield part of the sky (i.e. empty centers) and contaminate with their diffuse light the immediate vicinity (e.g. rings of points).

It allows to check whether either an XMM source is found in a masked region and then if any optical detection could be spoiled by this masking (e.g. XLSSC 029 on the upper left very border of the D1 Megacam field). Second, we give in Fig. 2 the various XMM-LSS fields along with their corresponding associated exposure times (which can vary by a factor of 2) along with the C1, 2 and 3 cluster detections. The part of the field at both small right ascension and declination with no XMM observations at all will be called the “Absence zone” in the following.

### 2.3. Galaxy density maps

The method is based on the simple detection of contrasts in numerical density maps of galaxies computed using  $i'$  band data. But, in order to eliminate as much as possible foreground contaminations, these density maps are built in redshift (distance) slices. The technique used to compute the galaxy density maps is the well known adaptive kernel method (see e.g. Dressler and Shectman 1988, Beers et al 1991 for seminal works and also Biviano et al. 1996 for a detailed application and discussion of significance). It has the advantage compared to wavelets (e.g. Escalera et al. 1992 or Slezak et al. 1994) of not needing reconstruction of the structures using the whole range of scales and is less affected by edge effects. Edge effects as well as mask effects (masks due for example to the presence of bright stars in the field) are not taken into account neither by mirroring the data nor by adding randomly distributed points. We compared our detections with the map of masks and eyeballed if there was any unfortunate coincidence. Systems where the center of the contours was in such a masked region were flagged by an (M) in the lists of candidates (if not already associated with an X-ray structure).

In this testing approach, we prefer to deal with crude artefacts rather to smooth them in order to estimate their effects when compared to totally different detection methods. In an application aimed at counting groups and clusters to constrain cosmology, it turns out that the best way would be to exclude totally and a posteriori masked regions as done e.g. when using lensing techniques. For the edge effects, comparison of our detections with real structures detected in X-ray will indicate in the following that the effect does not seem to be so important. Again, when counting structures, this should be taken into account by removing adequately border zones. Only foreseen comparison with simulations including fake structures where completeness in terms of richness or mass is well controlled, will allow quantitative estimates of these effects.

We thus define overlapping slices with width of 0.1 in photometric redshift all along the line of sight. An overlap of 0.05

is chosen as real structures are often expected to exhibit in adjacent slices.

The D1 field is  $0.8 \text{ deg}^2$  (after masked area rejection) and we define on it a grid of  $200 \times 200$  pixels. The pixel size ( $\sim 0.3$  arcmin) corresponds to  $\sim 80/120/160$  kpc at  $z=0.25/0.5/1$  and is left fixed with redshift.

In order to establish statistical significance, we use bootstrap technique both on real data and simulations. For each new realization of a given galaxy distribution obtained by the bootstrap technique we build the corresponding density map. In every new realization of the galaxy distribution, clustered points at “small” scales stay clustered but are however spread over. Points unclustered or clustered on larger scales are also spread over. Then, taking the mean of several density maps has the effect to erase fluctuations and flatten the mean background, letting clustering present. This flattening added to the removal of distant (or nearby) clustering due to the use of narrow slices allows the use of random distributions to evaluate false detections at least when using high value thresholds. In practice a “mean bootstrapped” map of the galaxy distribution within a given  $z_{\text{phot}}$  slice is obtained using 1000 bootstrap resamplings (see e.g. Biviano et al. 1996 for a complete description).

## 3. Application to real data and Reliability

### 3.1. Application to real data

The present analysis is performed using the  $i'$  band CFHTLS catalogue, down to the magnitude limit  $i' = 24.5$  which encompasses the typical  $i'^*$  of the luminosity function at  $z=1$  (e.g. Adami et al 2005) and which ensures a good compromise between going as red as possible and using the best quality photometric data.

We apply the technique to overlapping slices with central redshifts between 0.2 and 1.2 (where the quality of photometric redshifts is optimal). We add the slice 0.10-0.20 to check if the nearby C1/0.041 is detected by our method. We also give in appendix the tentative detections up to  $z=1.5$ , but these last results are still uncertain due to the decrease of the photometric redshift accuracy after  $z=1.2$ . This is also why the last redshift slice in appendix was taken larger (width of 0.15 in redshift) than the other ones.

Once for a given slice, the mean (from 1000 realizations obtained by bootstrapping the actual data) “image” (i.e. the mean galaxy density map) is obtained and a detection of the density peaks is performed on it. It uses the usual image analysis done with SExtractor (Bertin & Arnouts 1996) where the internal parameters are adapted to the pixel size with at least 2 pixels above the chosen threshold (3 or 4). As in usual image analyses, structures are detected with respect to their background (estimated globally in SExtractor) which defines a threshold (peak density over background density). Positions and best ellipse fitting (orientation and axes ratio) are derived adopting 1

Mpc as the size of the semi-major axis of the considered structures.

A catalogue of structures for each redshift slice is then generated. We also select individual galaxies potentially belonging to each structure as all galaxies included in the considered redshift slice and in the 1 Mpc semi-major axis ellipse. For a given structure, these lists still include, however, interloper galaxies that have positions inside the structure ellipse but are foreground or background galaxies included in the redshift slice. This is due to the photometric redshift uncertainty (see Ilbert et al. 2006).

We avoid the very low redshift slices because in that case, the number of expected structures is small due to the small solid angle and the reliability of photometric redshifts is degraded (see Ilbert et al. 2006). We also provide detections only up to  $z=1.2$  (tentative detections up to  $z=1.5$  are only given in appendix), but we clearly wait for complete comparison with the next generation of simulations to validate and study detections of the most distant candidate clusters in terms of mass. As we use galaxy as tracers of structures, it is important to deal with large scale structure simulations which include a well controlled implementation of galaxies and not only of DM. It is however encouraging that the number of detections agree well with generic GalICS predictions (see below).

Every significant (i.e in terms of threshold, see below) structure is labelled with an identification in every slice as well as a general identification. Some structures could show up at almost the same positions in several slices. In order to identify these multiple detections, we chose to give a single identification when two detections in adjacent redshift slices had overlapping ellipses on the sky. We show in Fig. 3 the coordinates differences of all multiple detections in successive redshift slices. This figure shows that two successive detections always are closer than 2Mpc (by definition) and that more than 75% are closer than 1Mpc. The values are of the order (or smaller) than 2 times the usual virial radius and this ensures that most of the time, we are not merging unrelated structures. The other detections of a given structure are then labelled by the same number but flagged by parentheses in Tabs. 3 to 5 which give a summary of the structures we found.

We note, however, that when a structure (e.g. large scale structure line-of-sight filaments) is percolating through a large number of redshift slices, the position of the lowest redshift detection can be quite different with the one in the highest redshift slice. We also note that C1-029 from Pierre et al. (2006) is just at the edge of the D1 field of view and is also located in a masked region. It is perhaps identified with the cluster 35 (general id of the tables), but this remains very uncertain.

Finally, as part of the D1 field is covered by VVDS data, we use the spectroscopic information. In every 1 Mpc ellipse, when available, we look at spectroscopic data in the 0.1 width redshift range to confirm if the local  $z$  distribution exhibits any compactness in the velocity space compatible with the presence of possible real structures. Namely, we looked at galaxies along the line of sight in the considered slice separated by gaps of less than 0.0026 (in order to use the same gap as in Adami et al. 2005 on similar spectroscopic data). These gaps were adapted to redshift using the  $(1+z)$  dependence.

**Table 1.** Number of peaks detected per square degree in 100 random fields (with 5000, 8000 and 11000 points each) with respect to a given threshold.

Threshold	5000 points	8000 points	11000 points
$\geq 3\text{-}\sigma$	$0.7\pm 0.8$	$0.6\pm 0.6$	$1.6\pm 0.9$
$\geq 4\text{-}\sigma$	$0.1\pm 0.2$	$0.2\pm 0.4$	$0.6\pm 0.6$

### 3.2. False detection rate evaluation

The first and main concern with any detection method is the question of false detections. Here we deal with that in the following way:

We generate 100 independent slices with 5000, 8000 and 11000 points randomly distributed (these numbers are representative of numbers of galaxies in real redshift slices as shown in tabs. 3 to 5) and we analyze these slices in the same way as real ones. We compute the number of detections depending on the detection thresholds used.

As we proceed in narrow slices, the effect of distant clustering which diminishes the contrast of real structures is also strongly diminished as well as with the bootstrapping. So, mean random fields are rather good representations of the actual slice background.

Table 1 shows the numbers of detections in a given slice (whatever the redshift) with respect to the threshold defined in terms of 3 and  $4\sigma$  of the (local) background. This table, then, gives an estimate of the level of wrong structure detections for a given slice. This level remains modest, since there is at most 2 in a given slice at the  $3\sigma$  level and 1 at the  $4\sigma$  level.

### 3.3. Global detection rate assessment with Galics simulations and other optical detection methods

As a first step we generate, using the 50 available GalICS simulations (with  $H_0 = 67 \text{ km.s}^{-1}.\text{Mpc}^{-1}$ ,  $\Omega_\Lambda = 0.67$  and  $\Omega_m = 0.33$ ), slices with the same widths as the ones with real data (e.g. Meneux et al. or Blaizot et al. 2006 for a discussion on the ability of these simulations to represent the real universe). These simulations are representative of the general clustering in the Universe all along with the same depth as our sample. For each GalICS slice we produce mean bootstrapped maps in the same conditions as for real data. In the present stage (see below), we will just check with these simulations that the used thresholds lead to a number of detections (see Tab. 2) not totally at odds with the ones provided by the real fields. Of course, as well in real data as in simulated ones, false detections (due e.g to projection effects) and cosmic variance affect the number of structures. Consequently, numbers are expected to agree only in the mean and we recall that a complete evaluation in terms of richness, mass and other characteristics is devoted to another paper.

We, however, compare from Tab. 2 and fig. 4 the number of detections in our sample and in the GalICS simulations. This will give a global estimate of how well our detections are in agreement with the cosmological model used in the chosen GalICS simulations. Fig. 4 shows that our number of detec-

**Table 2.** Number of peaks detected per square degree in 50 GalICS fields (averaged over the 50 available fields) and in real D1 fields (rescaled to 1 deg<sup>2</sup>) with respect to redshift and to a given threshold. We only give the non-overlapping redshift slices.

$z$	$\geq 3\sigma$ Gal	$\geq 4\sigma$ Gal	$\geq 3\sigma$ D1	$\geq 4\sigma$ D1
0.2-0.3	7.0±0.8	6.2±0.8	7.5	5.0
0.3-0.4	8.0±0.8	6.8±0.8	5.0	3.75
0.4-0.5	8.1±0.9	6.8±1.0	5.0	1.25
0.5-0.6	8.3±0.9	6.6±1.0	7.5	3.75
0.6-0.7	8.0±0.9	6.0±1.1	2.5	1.25
0.7-0.8	7.6±1.1	5.4±0.7	5.0	1.25
0.8-0.9	6.9±0.7	4.7±0.8	6.25	2.5
0.9-1.0	6.3±0.6	4.3±0.6	6.25	2.5
1.0-1.1	5.6±0.6	3.6±1.0	3.75	2.5
1.1-1.2	4.9±0.6	3.0±0.5	5.0	2.5
1.2-1.3	5.4±0.5	3.2±0.6	6.25	5.0

**Fig. 2.** Regions observed by XMM with the corresponding C1, C2 and C3 detections as in Fig. 1 (see Pierre et al 2006). The red circles have a shorter X-ray exposure time. Red filled squares are the C1 XMM-LSS clusters and blue ones are the C2 and C3.

tions is in good agreement with the ( $\Omega_\Lambda = 0.67$  and  $\Omega_m = 0.33$ ) model given the error bar sizes.

Of course these detections could be in both cases as well real or false detections. However, as seen above using the random fields representative of each slice background, the high level thresholds used show that the false detection rate is expected to be rather low. It would be an unlikely coincidence that in every slice, the number of real and false detections conspire to give the right numbers found.

We, however, note that we detect less structures at intermediate redshifts (0.55;0.75) than predicted by the model. But this corresponds also (see below) to a lack of X-ray detections revealing that it could be a real empty region. Finer comparisons are required in order to really constrain cosmology, but the relatively good agreement between simulations and observations gives confidence on the potentialities of the method.

As seen from tables 3 to 5, we detect, up to  $z=1.1$  about 40 independent structures within an area of 0.8 deg<sup>2</sup> which is very close to the 52±8 per deg<sup>2</sup> found by Olsen et al. (2007) using a totally different method and a slightly deeper magnitude limit (but given the considered magnitudes, this should only affect the faint population of our detected structures and not too strongly the structures themselves). A close comparison between the two methods is devoted to another paper.

### 3.4. Comparison with XMM-LSS and the VVDS

As we already said, the second concern (once false detection problem is addressed) is the ability of any method to detect real structures at the right place and at the right distance or rather to understand when and why they are not detected. In other words what is the so-called detection function associated?

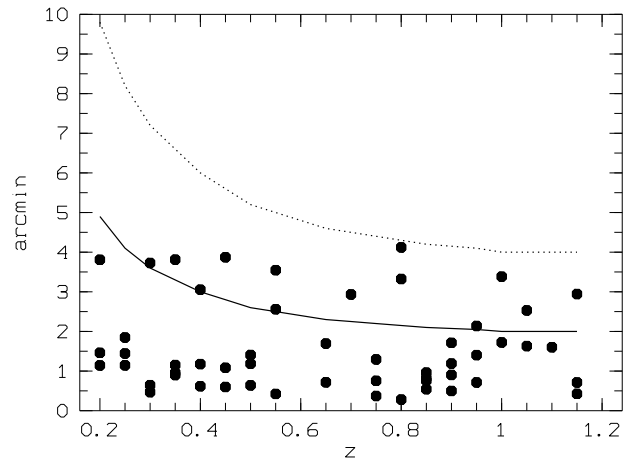


**Fig. 3.** Identification distance in arcmin between two detections (in successive redshift slices) that are assumed to be the same structure as a function of redshift. Solid and dashed lines are (in arcmin) the 1 and 2 Mpc values as a function of redshift.

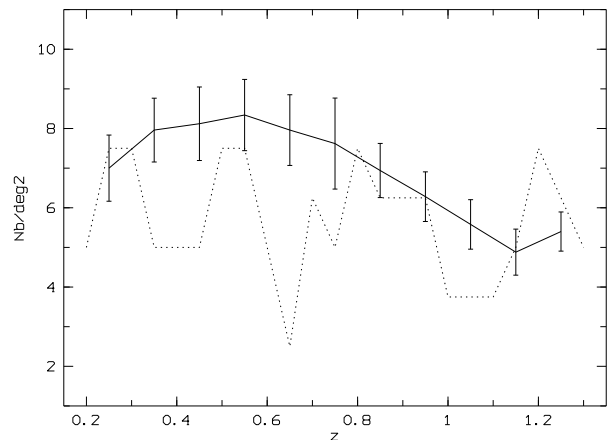


**Fig. 4.** Number of  $3\sigma$  detections per deg<sup>2</sup> in the GalICS simulations: continuous line with error bars. Number of detections per deg<sup>2</sup> in the D1 field: dashed line.

**Fig. 5.** Slice 0.10-0.20 (i.e.  $0.10 \leq z \leq 0.20$ ). Colour contours are drawn from the mean galaxy density image. Bottom level is the mean value of this density map. Black small dots show the fake galaxies detected in the D1 masked areas. Large circles are the XMM-LSS fields. Peaks are detected at the  $3\sigma$  level (check tables of structures to see which ones are also detected at the  $4\sigma$  level) and can be distinguished by their number. C1 XMM clusters (from Pierre et al. 2006) in the same redshift range (with an allowance of 0.01) are superimposed as red squares, C2 and C3 (from Pierre et al. 2006) as white squares. Coordinates are given in decimal degrees (J2000).

One way to estimate correctly such a selection function is the use of cosmological simulated catalogs analysed with exactly the same protocol as for the real data. One can also use mock catalogs in which structures are put by-hand allowing the recovery power estimation. However, if it is pedagogical in the

**Fig. 6.** Same as 5 for the slice 0.15-0.25.

**Fig. 7.** Same as 5 for the slice 0.20-0.30.

**Fig. 8.** Same as 5 for the slice 0.25-0.35.

**Fig. 9.** Same as 5 for the slice 0.30-0.40.

**Fig. 10.** Same as 5 for the slice 0.35-0.45.

**Fig. 11.** Same as 5 for the slice 0.40-0.50.

**Fig. 12.** Same as 5 for the slice 0.45-0.55.

**Fig. 13.** Same as 5 for the slice 0.50-0.60.

sense that it gives a flavour of how the algorithm works, it is not always possible to explore all the range of parameters and conditions in a practical way until detailed cosmological simulations adapted to the CFHTLS characteristics will be available.

A second way to estimate such a selection function is empirical: the use of detections obtained in a totally different way (X-ray emission of groups and clusters detected by the XMM-LSS) accounting in the meantime for spectroscopic information issued from VVDS. This spectroscopic information is used in the following way. For every structure in a given slice, we look at the redshift distribution of the VVDS data along the line of sight, within a 1 Mpc ellipse, up to  $z = 1.2$  (central redshift of the highest redshift considered slice) and we look for clustering in spectroscopic redshift within the redshift range of the slice. We put galaxies as possible members of a system when the redshift of 2 galaxies do not differ by more than  $0.0026 \times (1 + z)$  (see also Section 3.1). All the corresponding numbers of this analysis are given in table 6.

Here, we check if, with the thresholds defined above, we recover or not the various XMM sources. Of course, there are physical reasons for not detecting in X-ray an optical overdensity (e.g. if dealing with a non totally virialized system) as well as observational ones since XMM-LSS does not cover entirely D1 and has not a completely homogeneous exposure time. Conversely, if there is no optical structure when a diffuse X-ray source is present, it could reveal a failure of the present method or a mistake in its distance as well as a peculiar class of extended X-ray structures (as fossil groups that are galaxy-very-poor massive systems, e.g. Jones et al. 2003 or Ulmer et al. 2005).

Figures 5 to 23 show a subsample of the slices up to  $z = 1.1$  for thresholds of  $3\sigma$ . We note that these figures are plotted with the same color coding, with the lowest level being the mean value of the density map. If different slices exhibit strongly different background noise (or different maximal density values), then, significant peaks can appear less prominent in the figures compared to less significant peaks in slices with different noise level. The individual properties of the structures are given in Tabs. 3 to 5.

We overplotted XMM-LSS clusters in the range 0.1 - 1.2 with the following rule: C1, C2 and C3 XMM-LSS clusters were plotted in our graphs when included in the considered photometric redshift range (with an allowance of 0.01, only useful for C1-025).

In the tables, when a given structure is detected in adjacent slices, to identify it with an X-ray source, we always select

the one corresponding to the highest significance level. The X-ray position has to be included in the optical detection ellipse. Finally, in the tables, we also take into account the XMM-LSS clusters provided by Andreon et al. (2005) and Willis et al. (2005) in particular analyses, separate from Pierre et al. (2006), but using the same XMM data.

- First, it should be noted that for redshift higher than 0.1 all XMM-LSS C1 clusters are detected at the  $3\sigma$  level with the present method (except for C1-029 almost outside the optical field and in a masked region of this field). Most of these are also detected at the  $4\sigma$  level except C1-005 (detected at the  $3.75\sigma$  level) and C1-025 (at  $3.3\sigma$  level).
- C2-038 is not detected in our analysis and is neither in a masked nor in an edge region. Looking in more detail at the maps shows that it is detected at only a  $1.5\sigma$  level in the [0.50;0.60] slice.
- We also detect 2 out of the 4 C3 clusters. Surprisingly, the C3 detected are at high  $z$  while the non-detected ones are at low redshift. However, C3-a appears close to a bright star and is probably spoiled in the CFHTLS data (masked region). For C3-d, it appears also to be detected at only  $1.5\sigma$  in the [0.30;0.40] slice.
- We finally find coincidence in the correct redshift range (see Tabs. 3 to 5) for structures 4 and 34 with the X-ray sources confirmed by Andreon et al. (2005) and Willis et al. (2005).
- It must be underlined that our analysis succeed to recover afterwards the cluster 0004 (number 15) of the [0.50;0.60] redshift slice, identified as a faint X-ray source but rejected as a possible extended source from the XMM-LSS list in a first stage (so not included in the C1/C2/C3 classification). This X-ray source is very close to the bright XMM-LSS C1 cluster 041 but is still detected by our method (see Figs. 12 and 26). This illustrates the ability of our method to efficiently disentangle nearly superposed clusters. We also found detections apparently without any X-ray identification. One clear example is given by structure 12 detected here at the  $3\sigma$  level without confirmed X-ray counterpart in the redshift bin. For this region, however, more than 30 VVDS redshifts are available confirming real clustering at  $z \sim 0.31$ .

In summary, there are 1 C2 cluster and 2 C3 clusters that are not detected at the  $3\sigma$  level (but 2 are recovered at lower levels) with no obvious explanation among the confirmed clusters from Pierre et al. (2006). This corresponds to a level of

**Fig. 14.** Same as Fig. 5 for the slice 0.55-0.65.

**Fig. 15.** Same as Fig. 5 for the slice 0.60-0.70.

**Fig. 16.** Same as Fig. 5 for the slice 0.65-0.75.

**Fig. 17.** Same as Fig. 5 for the slice 0.70-0.80.

~15% which turns out to be the number of completely missed structures by our method compared to X-ray methods.

Conversely, as said above, several structures are detected in the visible at a significant level with no counterparts in X-ray. Are they real or are they false detections? Restricting to areas in common, with no biases (i.e. excluding A,G,E,M,S regions: see Tabs. 3 to 5) and limiting ourselves to  $z \leq 1.05$  (the limit in redshift of Pierre et al. 2006) we find 11 such structures of which 5 have spectroscopic information. Namely these are systems 2, 16, 19, 21 and 28 (see Tab. 6) and are therefore likely to be real. We also note that structure number 3 (general id) is detected at  $z=0.26$  by Pierre et al. (2006) and at  $z=0.225$  using only VVDS redshifts. This discrepancy is probably due to the small number of VVDS redshifts (4) in the considered slice leading to a wrong estimate.

We conclude that we are probably more efficient to detect very low mass and galaxy-dominated systems (as compared with gas or dark matter dominated systems) compared to X-ray methods. These 11 only optically detected structures is the number of probably missed structures by the X-ray method.

### 3.5. Clusters, groups and filament properties

A future paper will be dedicated to the precise study of the properties of these structures but we show in Fig. 24 the histogram of all photometric redshifts along the line of sight between  $z=0.1$  and 1.25 overplotted with detected structures. We clearly see that we detect structures in almost all galaxy concentrations in the redshift space. We also detect several structures in low density regions.

We also present an example of what can be done. Fig. 25 shows for example the luminosity functions in the CFHTLS  $u^*$ ,  $g^*$ ,  $r^*$ ,  $i^*$  and  $z^*$  bands of the candidate 0004 in the [0.25;0.35] redshift slice. Objects are selected in the slice (so we still have some foreground and background contamination by galaxies in the considered slice but not physically included in the structures) and within the 1 Mpc ellipse. It also shows the redshift and spectro-morphological type histograms (following Coleman et al. 1980) as well as the red sequence in the Colour Magnitude Relation.

Another remark concerns the detection of structures showing up in several redshift slices. Two such structures (limit-

**Fig. 18.** Same as Fig. 5 for the slice 0.75-0.85.

**Fig. 19.** Same as Fig. 5 for the slice 0.80-0.90.

**Fig. 20.** Same as Fig. 5 for the slice 0.85-0.95.

**Fig. 21.** Same as Fig. 5 for the slice 0.90-1.00.

**Fig. 22.** Same as Fig. 5 for the slice 0.95-1.05.

**Fig. 23.** Same as Fig. 5 for the slice 1.00-1.10.

ing ourselves to the non heavily polluted by CFHTLS masking candidates and to  $z$  lower than 1.05: structures 4 and 23) extend over redshift intervals of strictly more than 0.3 and are detected in each of the successive bins at the  $3\text{-}\sigma$  level (see Tab. 7). This interval of 0.3 represents  $\pm 3$  times the typical photometric redshift uncertainty. It is also also larger than the catastrophic errors. This ensures us that we are probably not dealing with artefacts. It can still be chance alignments of real structures. However, if not, this is really a puzzling fact as the length of these filaments (or structure chains) is several hundreds of Mpc! Their radial extension is clearly larger than the maximal void sizes computed in Hoyle & Vogeley (2004). If these filaments are real, then they have to cross at least one node (the place where the massive clusters form) of the cosmic web and to percolate from a cosmic cell to another one. We should therefore detect massive clusters inside these filaments in the XMM-LSS data and these are, indeed, associated with X-ray structures.

## 4. Conclusions

We show in this paper that using the excellent quality photometric redshifts computed on the D1 CFHTLS field by Ilbert et al. (2006) and combining them with an adaptive kernel galaxy density estimate, we are able to efficiently detect structures up to  $z \sim 1.05$  without any hypotheses on the nature of what the structures are.

The analysis based on slices in redshift space allows to reduce efficiently foreground and background contamination, then increasing the contrast of real structures.

Our detections, taking into account biases of both analyses, are in good agreement with X-ray detections (and sometimes help to recover them) and also allow to detect low mass structures, invisible for X-ray surveys. Detections with no evident X-ray counterpart are in general confirmed by spectroscopic information when available. The efficiency of the method seems to be due also to the fact that light appears to trace mass in clusters which has been verified at least for small redshifts (e.g.

**Table 7.** Redshift detection interval of the radial filaments, mean coordinates, X-ray association, redshift extension in Mpc and redshift extension in Mpc quadratically diminished with the  $\pm 1\sigma$  photometric redshift uncertainty at the given redshift.

z det. int.	$\alpha$	$\delta$	X-ray	red. ext.	corr. ext.
1.15 - 0.60	36.25	-4.20	yes	1467 Mpc	1421 Mpc
0.60 - 0.15	36.60	-4.05	yes	1632 Mpc	1581 Mpc

**Table 3.** From a central redshift of 0.15 to 0.70. Structures detected along with their redshift slice (and the total number of galaxies inside the slice), structure id, coordinates, minimum detection level, general identification, X-ray association (redshift coming from Pierre et al. 2006, Willis et al. 2005 or Andreon et al. 2005) or (if not identified in the slice or in another slice) reason potentially explaining the absence of X-ray detection (center of the structure located in A: the Absence zone, G: a Gap between two X-ray pointings, M: a region strongly affected by Masked CFHTLS areas, S: a single XMM field where the exposure time was Short, E: a region with an X-ray detection very close to the CFHTLS D1 field Edge), X-ray temperature when available and VVDS redshifts available (Yes or No). Some structures show up at almost the same positions in several slices: the secondary detections are then labelled by the same number but flagged by parentheses (the unflagged number is the detection made with the highest signal to noise). W05 refers to Willis et al. (2005) and A05 to Andreon et al. (2005).

Slice	id	$\alpha$	$\delta$	Min. thres.	gen. id.	X-ray id and z XMM	T-X	VVDS
0.10-0.20 (5868)	0001	36.3789	-4.2424	4	1	C1-041/0.14	1.3 keV	Y
	0002	36.7981	-4.1970	3	2			Y
0.15-0.25 (7848)	0001	36.3746	-4.6831	3	3	C1-025/0.26	2.0 keV	Y
	0002	36.5767	-4.0699	3	(4)	S		N
	0003	36.6240	-4.2523	3	5	S		Y
	0004	36.8215	-4.5465	3	(6)	S		Y
0.20-0.30 (9252)	0001	36.8946	-4.8679	4	7	C1-022/0.29	1.7 keV	N
	0002	36.2451	-4.8901	3	8	A/M		N
	0003	36.1364	-4.2134	4	9	C1-044/0.26	1.3 keV	
	0004	36.6840	-4.2315	3	(5)			Y
	0005	36.8435	-4.5570	4	(6)			Y
	0006	36.5928	-4.0801	4	(4)	S		N
0.25-0.35 (10570)	0001	36.3166	-4.7515	3	10	MA		Y
	0002	36.9117	-4.8594	4	(7)			N
	0003	36.6381	-4.8759	4	11	M		N
	0004	36.8416	-4.5810	4	6	C1-013/0.31	1.0 keV	Y
	0005	36.6121	-4.0741	3	(4)			N
	0006	36.6104	-4.5286	3	12	S		Y
0.30-0.40 (9973)	0001	36.2974	-4.7511	3	(10)	A/M		Y
	0002	36.6445	-4.8804	4	(11)	M		N
	0003	36.8090	-4.6339	4	(6)	G/M		Y
	0004	36.6215	-4.0689	4	4	XLSS014/W05/0.34		N
0.35-0.45 (8248)	0001	36.1413	-4.8965	4	13	A/M		N
	0002	36.6542	-4.9432	4	(11)	G		N
	0003	36.7937	-4.6294	3	(6)	G/M/S		Y
	0004	36.6156	-4.0665	3	(4)	S		N
0.40-0.50 (8302)	0001	36.1201	-4.8502	4	(13)	A		N
	0002	36.6735	-4.9467	4	(11)	G		N
	0003	36.0884	-4.0633	3	(14)			N
	0004	36.6258	-4.0680	3	(4)	S		N
0.45-0.55 (9216)	0001	36.1152	-4.8328	4	(13)	A		N
	0002	36.6799	-4.0610	3	(4)	G		N
	0003	36.0798	-4.0684	4	14			N
	0004	36.3842	-4.2726	4	15	S		Y
	0005	36.8975	-4.3768	3	16			Y
	0006	36.8481	-4.6202	3	17	G/M		Y
0.50-0.60 (10201)	0001	36.1202	-4.8557	4	(13)	A		N
	0002	36.6990	-4.0559	3	(4)			N
	0003	36.0758	-4.1999	4	18	M		N
	0004	36.3762	-4.2655	4	(15)	S		Y
	0005	36.8334	-4.4982	3	(19)	M		Y
	0006	36.2840	-4.7423	3	20	A/M		N
0.55-0.65 (10845)	0001	36.1366	-4.8951	3	(13)	A		N
	0002	36.3825	-4.2687	3	(15)	S		Y
	0003	36.4645	-4.4997	3	21			Y
	0004	36.8646	-4.5484	4	19			Y
0.60-0.70 (10224)	0001	36.6686	-4.5096	4	22	S		Y
	0002	36.2364	-4.2232	3	(23)			N
0.65-0.75 (9243)	0001	36.0853	-4.7942	3	24	A		N
	0002	36.4815	-4.0820	3	25	M/S		N
	0003	36.7546	-4.0752	3	26			N
	0004	36.2823	-4.2157	3	27			Y

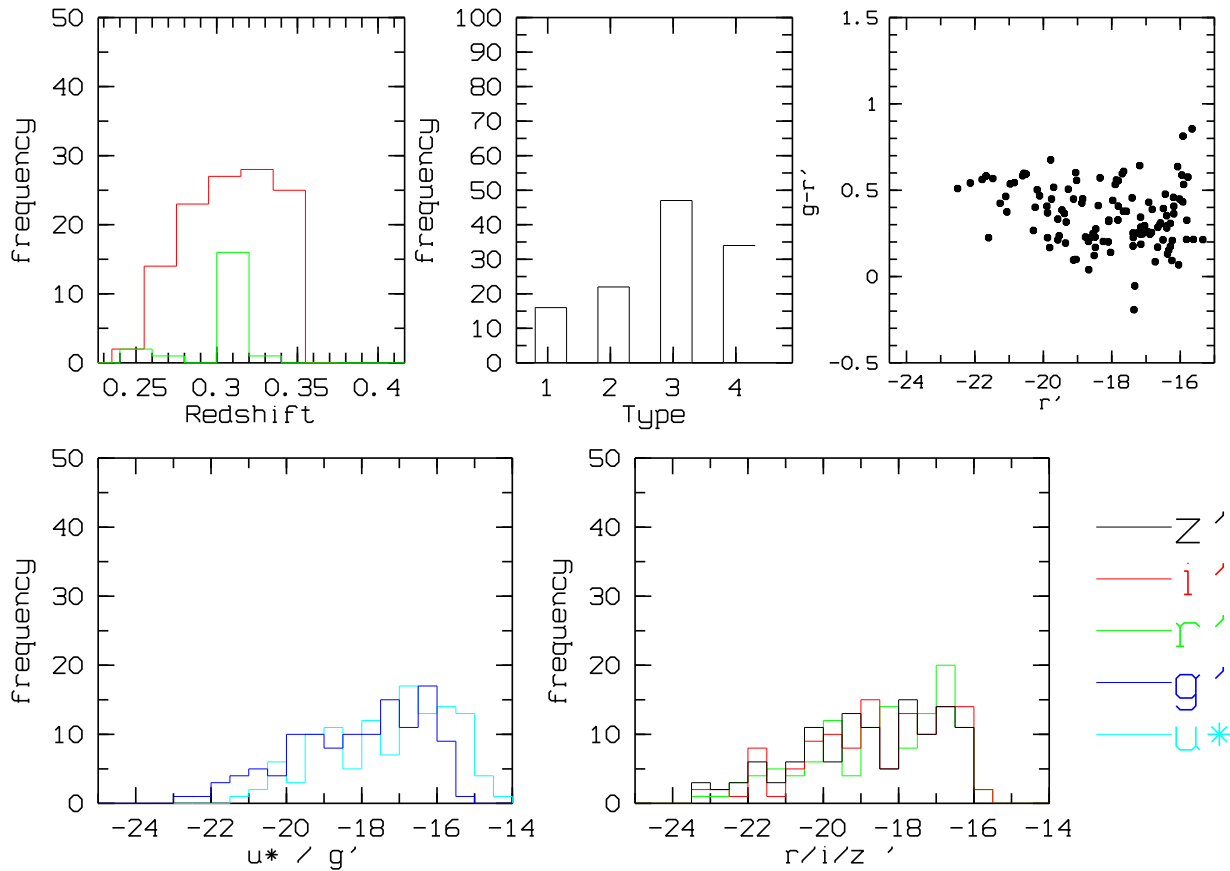


**Fig. 25.** Summary of the properties for the candidate 0004 in the [0.25;0.35] redshift slice. Lower left:  $u^*$  and  $g'$  band absolute magnitude histograms, lower right:  $r'$ ,  $i'$ ,  $z'$  absolute magnitude histograms, upper left: redshift histograms (photometric redshifts: red, spectroscopic redshifts: green), upper center: spectrophotometric types (following Coleman et al. 1980), upper right: colour magnitude relation.

Katgert et al. 2004). It is then encouraging in this perspective to use our method in parallel with others to count clusters both in simulations with realistic galaxy representation and in the real universe. We detect at least two structure-chains of several hundreds of Mpc (structures 4 and 23). The size of the D1 field is, however, far too small to conduce quantitative cosmological studies, but it allows to calibrate our method. Such quantitative studies will be achieved in future works using other large scale and deep CFHTLS fields.

*Acknowledgements.* The authors thanks C. Benoist and L.F. Olsen for useful discussions. This work is based in part on data obtained with the European Southern Observatory on Paranal, Chile, and on observations obtained with MegaPrime/Megacam, a joint project of CFHT and CEA/DAPNIA, at the Canada France Hawaii Telescope (CFHT) which is operated by the National Research Council (NRC) of Canada, the Institut National des Science de l'Univers of the Centre National de la Recherche Scientifique (CNRS) of France, and the University of Hawaii. This work is based in part on data products produced at TERAPIX and the Canadian Astronomy Data Centre as part of the Canada-France-Hawaii Telescope Legacy Survey, a collaborative project of NRC and CNRS. This work is based in part on observations obtained with XMM-Newton, an ESA science mission with instruments and contributions directly funded by ESA Member states and

NASA. The VLT-VIMOS observations have been carried out on guaranteed time (GTO) allocated by the European Southern Observatory (ESO) to the VIRMOS consortium, under a contractual agreement between the Centre National de la Recherche Scientifique of France, heading a consortium of French and Italian institutes, and ESO, to design, manufacture and test the VIMOS instrument.

## References

- Adami, C., Mazure, A., Ilbert, O. et al, 2005, *A&A*, 443, 805
- Andreon S., Valtchanov I., Jones L.R., et al., 2005, *MNRAS* 359, 1250
- Beers T.C., Gebhardt K., Forman W., Huchra J.P., Jones C., 1991, *AJ* 102, 1581
- Bertin E., Arnouts S., 1996, *A&AS* 124, 163
- Biviano A., Durret F., Gerbal D., et al., 1996, *A&A* 311, 95
- Blaizot J., Szapudi I., Colombi S., et al., 2006, *MNRAS* 369, 1009
- Coleman G.D., Wu C.C., Weedman D.W., 1980, *ApJS* 43, 393
- Cucciati O., Iovino A., Marinoni C., et al., 2006, *A&A* 458, 39
- Dressler, A., Shectman, S.A., 1988, *AJ*, 95, 985
- Escalera E., Mazure A., 1992, *ApJ* 388, 23
- Forbes D.A., Ponman T., Pearce F., et al., 2006, *PASA* 23, 38
- Gavazzi, R., Soucail, G., astro-ph/0605591
- Gladders, M.D., Yee, H.K.C., 2005, *ApJS* 157, 1
- Gladders, M.D., Yee, H.K.C., 2000, *AJ* 120, 2148

**Table 4.** From central redshift of 0.75 to 1.05. We note that structure 35 (general identification) is present from  $z=0.85$  to  $z=1.25$  with a small position shift on the sky. Structure 29 (general identification) is perhaps identified with C3-c cluster (Pierre et al. 2006) but the case is not closed as it is located very close to a masked region.

Slice	id	$\alpha$	$\delta$	Threshold in $\sigma$	gen. id.	X-ray id and z XMM	T-X	VVDS
0.70-0.80 (9585)	0001	36.9250	-4.9052	3	27	M		N
	0002	36.1835	-4.1749	4	(23)			N
	0003	36.8791	-4.2025	3	28			Y
	0004	36.4924	-4.4782	3	(29)			Y
0.75-0.85 (9741)	0001	36.0853	-4.8695	3	(30)	A		N
	0002	36.7614	-4.0793	3	31			N
	0003	36.1627	-4.1807	4	(23)			N
	0004	36.8789	-4.2087	3	(28)			Y
	0005	36.7091	-4.2481	3	32			N
	0006	36.5030	-4.4714	3	29	C3-c/0.82 ?		Y
0.80-0.90 (11004)	0001	36.0856	-4.8648	4	30	A		N
	0002	36.8458	-4.1485	3	(28)			Y
	0003	36.3781	-4.1865	3	33	S		N
	0004	36.2113	-4.2073	3	(23)			N
	0005	36.4003	-4.4181	4	(34)			Y
0.85-0.95 (12019)	0001	36.0864	-4.8774	3	(30)	A		N
	0002	36.0587	-4.2291	3	(35)	M		N
	0003	36.3895	-4.1940	4	(33)	S		N
	0004	36.2141	-4.2231	3	(23)			N
	0005	36.3925	-4.4135	4	34	XLSSJ022534.2/A05/0.92 C3-b/0.92		Y
0.90-1.00 (11658)	0001	36.0983	-4.8933	4	(30)	A		N
	0002	36.0664	-4.2379	3	(35)	M		N
	0003	36.2245	-4.2340	3	(23)			N
	0004	36.2492	-4.3086	4	36			N
	0005	36.3847	-4.4106	3	(34)			Y
0.95-1.05 (9998)	0001	36.0989	-4.9052	3	(30)	A		N
	0002	36.0872	-4.2272	4	35	E		N
	0003	36.2499	-4.2590	4	(23)			N
1.00-1.10 (8203)	0001	36.7801	-4.2833	3	37	C1-005/1.05	3.7 keV	N
	0002	36.0875	-4.1856	4	(35)	E		N
	0003	36.2513	-4.2303	4	(23)			N

**Table 5.** From a central redshift of 1.10 to 1.20.

Slice	id	$\alpha$	$\delta$	Threshold in $\sigma$	gen. id.	X-ray id and z XMM	T-X	VVDS
1.05-1.15 (7755)	0001	36.2635	-4.2060	3	(23)			N
	0002	36.8640	-4.2023	3	38			N
	0003	36.0848	-4.2277	3	(35)	M		N
1.10-1.20 (7612)	0001	36.5663	-4.8823	4	39			N
	0002	36.9197	-4.9233	3	40	M		N
	0003	36.0714	-4.2046	4	(35)	M		N
	0004	36.9054	-4.1090	4	41			N
1.15-1.25 (7662)	0001	36.5183	-4.8925	4	(39)			N
	0002	36.9264	-4.9257	4	(40)	M		N
	0003	36.0635	-4.2135	4	(35)	M		N
	0004	36.9042	-4.4438	3	42			Y
	0005	36.8769	-4.6289	4	43	M/G		Y
	0006	36.0565	-4.0944	3	44			N

Hamana T., Miyazaki S., Shimasaku K., et al., ApJ, 2003 597, 98  
 Hoyle F., Vogeley M.S., 2004, ApJ 607, 751  
 Ilbert O., Arnouts S., McCracken H.J., et al., 2006, A&A 457, 841  
 Jones L.R., Ponman T.J., Horton A., et al., 2003, MNRAS 343, 627  
 Katgert P., Biviano A., Mazure A., 2004, ApJ 600, 657  
 Le Fèvre O., Vettolani G., Garilli B., et al., 2005, A&A 439, 845  
 Meneux B., Le Fèvre O., Guzzo L., et al., 2006, A&A 452, 387  
 Miller C.J., Nichol R.C., Reichart D., et al., 2005, AJ 130, 968

Olsen L.F., Benoist C., Cappi A., et al., 2007, A&A 461, 81  
 Postman M., Lubin L.M., Gunn J.E., et al., 1996, AJ 111, 615  
 Pierre M., Pacaud F., Duc P.-A., et al., 2006, MNRAS 372, 591  
 Slezak E., Durret F., Gerbal D., 1994, AJ 108, 1996  
 Tang J.Y., Fan Z.H., 2005 ApJ, 635, 60  
 Ulmer M.P., Adami C., Covone G., et al., 2005, ApJ 624, 124  
 Willis J.P., Pacaud F., Valtchanov I., et al., 2005, MNRAS 363, 675

**Table 6.** Main structures detected and with VVDS spectroscopic data, id, coordinates, general identification, Nb of redshifts in the slice, Nb of redshifts in the system (when two systems are visible, we give both values), central redshift, velocity dispersion (when more than 4 available redshifts). We restrict here to VVDS redshift selected in the ellipse corresponding to every structure. When no value is given for the mean redshift and velocity dispersion, this means that the sparse sampling and/or the small number of data do not allow a significant characterization.

Slice	id	$\alpha$	$\delta$	gen. id.	N-slice	N-St	zcentral	$\sigma_v$ (km/s)
0.10-0.20	0001	36.3789	-4.2424	1	3	2	0.138	
	0002	36.7981	-4.1970	2	3	2	0.185	
0.15-0.25	0001	36.3746	-4.6831	3	4	2	0.225	
	0003	36.6240	-4.2523	5	11	5	0.210	258
0.25-0.35	0001	36.3166	-4.7515	10	3	3	0.311	
	0004	36.8416	-4.5810	6	12	6	0.308	391
	0006	36.6104	-4.5286	12	30	21	0.313	727
0.45-0.55	0004	36.3842	-4.2726	15	2	2	0.542	
	0005	36.8975	-4.3768	16	2	1	0.53	
	0006	36.8481	-4.6202	17	4	3	0.543	
0.55-0.65	0003	36.4645	-4.4997	21	15	9	0.613	594
	0004	36.8646	-4.5484	19	10	6	0.610	864
0.60-0.70	0001	36.6686	-4.5096	22	15	7/6	0.634/0.687	319/601
0.70-0.80	0003	36.8791	-4.2025	28	2	2	0.784	
0.75-0.85	0006	36.5030	-4.4714	29	2			
0.85-0.95	0005	36.3925	-4.4135	34	10	5	0.920	488

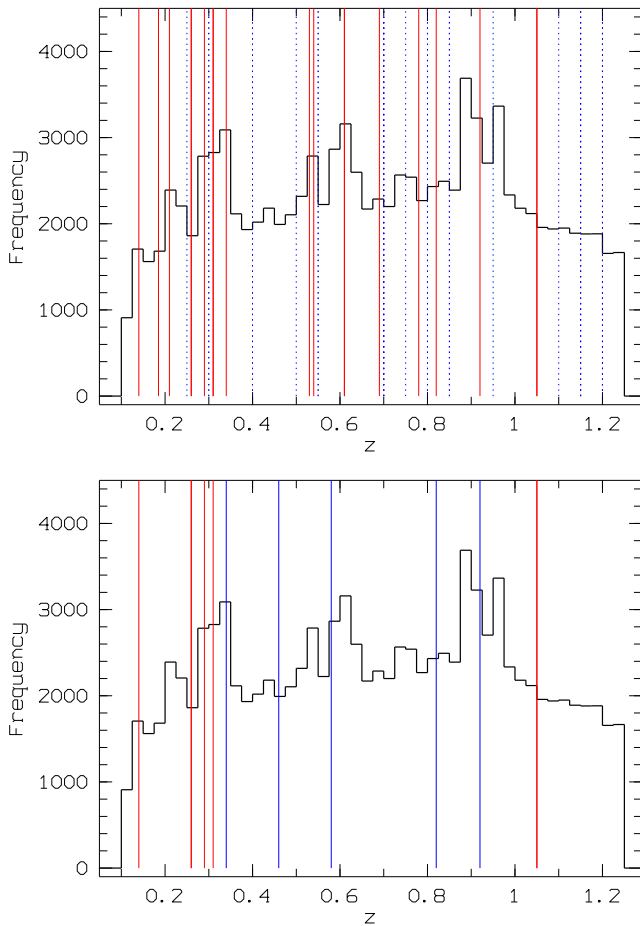


**Fig. 24.** Histogram of all photometric redshifts along the line of sight between  $z=0.1$  and  $1.25$  overlotted with detected structures.

Upper figure: structures detected with the photometric redshifts. Those with a precise redshift determination (first from XMM-LSS papers and second from VVDS spectroscopic data) are the red continuous lines. The blue dashed lines are clusters with only the photometric redshift determination (taken as the central redshift of the considered slice).

Lower figure: structures detected in X-rays from Pierre et al. (2006). C1 clusters are the red lines. C2 and C3 clusters are the blue lines.

**Fig. 26.** Trichromatic  $r/i/z$  CFHTLS image of candidate 0004 in the slice  $0.50-0.60$ . The three XMM-LSS spectroscopic redshifts (distinct from the 2 VVDS redshifts) are shown. The large galaxy to the top of the image is related to the XMM-LSS C1 cluster 041 at  $z=0.14$ .

# Online Material

**Table .1.** Same as Tabs. 3 to 5 for slices with central redshifts between 1.25 to 1.425.

Slice	Structure id	$\alpha$	$\delta$	Threshold in $\sigma$	gen. id.	X-ray id and z XMM	T-X	VVDS	Nb
1.20-1.30 (7174)	0001	36.9239	-4.9189	4	(40)	M		N	
	0002	36.4878	-4.9125	4	(39)			N	
	0003	36.9052	-4.4377	4	(42)			Y	1
	0004	36.8669	-4.6201	4	(43)	M/G		N	
	0005	36.0596	-4.0896	3	(44)			N	
1.25-1.35 (6352)	0001	36.7340	-4.7891	4	45			N	
	0002	36.0588	-4.1025	3	(44)			N	
	0003	36.8989	-4.4477	4	(42)			N	
	0004	36.8744	-4.6244	3	(43)	M/G		N	
1.30-1.40 (5004)	0001	36.7386	-4.7950	4	(45)			N	
	0002	36.8913	-4.4610	3	(42)			Y	1
1.35-1.50 (5673)	0001	36.8357	-4.6087	3	46	M/G		N	
	0002	36.3528	-4.1316	3	47	S		N	
	0003	36.9115	-4.4723	3	(42)			N	

This figure "D1-010-020-im3sig.jpg" is available in "jpg" format from:

<http://arxiv.org/ps/astro-ph/0702430v1>

This figure "D1-015-025-im3sig.jpg" is available in "jpg" format from:

<http://arxiv.org/ps/astro-ph/0702430v1>

This figure "D1-020-030-im3sig.jpg" is available in "jpg" format from:

<http://arxiv.org/ps/astro-ph/0702430v1>

This figure "D1-025-035-im3sig.jpg" is available in "jpg" format from:

<http://arxiv.org/ps/astro-ph/0702430v1>

This figure "D1-030-040-im3sig.jpg" is available in "jpg" format from:

<http://arxiv.org/ps/astro-ph/0702430v1>

This figure "D1-035-045-im3sig.jpg" is available in "jpg" format from:

<http://arxiv.org/ps/astro-ph/0702430v1>

This figure "D1-040-050-im3sig.jpg" is available in "jpg" format from:

<http://arxiv.org/ps/astro-ph/0702430v1>

This figure "D1-045-055-im3sig.jpg" is available in "jpg" format from:

<http://arxiv.org/ps/astro-ph/0702430v1>

This figure "D1-050-060-im3sig.jpg" is available in "jpg" format from:

<http://arxiv.org/ps/astro-ph/0702430v1>

This figure "D1-055-065-im3sig.jpg" is available in "jpg" format from:

<http://arxiv.org/ps/astro-ph/0702430v1>

This figure "D1-060-070-im3sig.jpg" is available in "jpg" format from:

<http://arxiv.org/ps/astro-ph/0702430v1>

This figure "D1-065-075-im3sig.jpg" is available in "jpg" format from:

<http://arxiv.org/ps/astro-ph/0702430v1>

This figure "D1-070-080-im3sig.jpg" is available in "jpg" format from:

<http://arxiv.org/ps/astro-ph/0702430v1>

This figure "D1-075-085-im3sig.jpg" is available in "jpg" format from:

<http://arxiv.org/ps/astro-ph/0702430v1>

This figure "D1-080-090-im3sig.jpg" is available in "jpg" format from:

<http://arxiv.org/ps/astro-ph/0702430v1>

This figure "D1-085-095-im3sig.jpg" is available in "jpg" format from:

<http://arxiv.org/ps/astro-ph/0702430v1>

This figure "D1-090-100-im3sig.jpg" is available in "jpg" format from:

<http://arxiv.org/ps/astro-ph/0702430v1>

This figure "D1-095-105-im3sig.jpg" is available in "jpg" format from:

<http://arxiv.org/ps/astro-ph/0702430v1>

This figure "D1-100-110-im3sig.jpg" is available in "jpg" format from:

<http://arxiv.org/ps/astro-ph/0702430v1>

This figure "figcand.jpg" is available in "jpg" format from:

<http://arxiv.org/ps/astro-ph/0702430v1>

This figure "figxmmdet.jpg" is available in "jpg" format from:

<http://arxiv.org/ps/astro-ph/0702430v1>

This figure "figxmmdetmask.jpg" is available in "jpg" format from:

<http://arxiv.org/ps/astro-ph/0702430v1>